

## Viscoelastic reverse time migration with attenuation compensation

Tieyuan Zhu<sup>1</sup> and Junzhe Sun<sup>2</sup>

### ABSTRACT

We have developed a theory of viscoelastic reverse time migration (RTM). The main feature of viscoelastic RTM is a compensation for P- and S-wave attenuation effects in seismic images during migration. The forward modeling engine is based on a viscoelastic wave equation involving fractional Laplacians. Because of the decoupled attenuation property, wave propagation can be simulated in three scenarios, i.e., only the amplitude loss effect, only the phase dispersion effect, or both effects simultaneously. This separation brings practical flexibility to studying attenuation effects on wave propagation and imaging. The backward modeling operator is constructed by reversing the sign of first-order time derivative amplitude loss operators. Synthetic examples determine the ability of viscoelastic RTM to illuminate degraded areas and shadow zones caused by attenuation. Numerical experiments also reveal that  $Q$ -compensated imaging is noticeably more accurate in kinematics and dynamics than elastic imaging in the presence of high attenuation. Results from a synthetic 3D model determine the superiority of viscoelastic RTM over elastic RTM in imaging salt flanks and delineation of salt boundaries, which are dimmed in elastic images.

### INTRODUCTION

Elastic imaging using multicomponent seismic data is an important technique for mapping subsurface geologic structures (Stewart et al., 2002; Hardage et al., 2011). Compared with acoustic imaging, the advantage of elastic imaging is the ability to provide more informative characterization of the subsurface (including P-, S-, and converted waves). The resulting elastic images have been used widely for geologic interpretation. For example, the converted wave

image delineated the base of the gas-charged channels and even internal structures where the P-wave signal is attenuated through gas-charged channels (Li et al., 2007). They were also used to provide an estimation of  $V_P/V_S$  parameter for reservoir monitoring and to detect fractures through S-wave splitting in anisotropic media (e.g., Stewart et al., 2002; Hardage et al., 2011; Liu and Martinez, 2013). Traditional elastic imaging techniques, e.g., Kirchhoff migration and reverse time migration (RTM) based on the elastic wave equation, assume no attenuation in the subsurface (e.g., Kuo and Dai, 1984; Chang and McMechan, 1987; Hokstad, 2000; Yan and Sava, 2008).

However, it has been well-recognized that seismic waves propagating in the subsurface are attenuated, particularly in exploration reservoir areas, e.g., fluid-filled fractures and the presence of free gas accumulations in shallow sediments. These areas often exhibit strong seismic attenuation (i.e., a low quality factor  $Q$ ). Mavko et al. (2005) observe extremely strong P-wave attenuation ( $1/Q$ ), ranging between  $Q = 5$  and 10, in gas sands from the Gulf coast. Klimentos (1995) reports that S-wave attenuation is approximately the same as the P-wave attenuation in liquid-saturated sandstone. Consequently, recorded P- and S-waves in these areas are significantly affected in amplitude and phase, leading to degraded seismic images (e.g., shadow zones) as a result of missing high wavenumbers. Here, we limit our focus on intrinsic attenuation, although seismic scattering attenuation caused by heterogeneity also complicate amplitude analysis (Browaeys and Fomel, 2009). In addition, migration amplitude information is desirable for quantitative seismic processing, e.g., amplitude variation with offset/amplitude variation with amplitude analysis. This motivates to develop an accurate viscoelastic imaging approach that mitigates the effects of P- and S-waves attenuation.

Most recent efforts have been made to incorporate acoustic attenuation effects in seismic processing and migration (Deng and McMechan, 2007; Zhang et al., 2010, 2013; Fletcher et al., 2012; Dutta and Schuster, 2014; Shen et al., 2014; Zhu et al., 2014; Sun et al., 2015). Some of these algorithms have been tested using real

Manuscript received by the Editor 5 May 2016; revised manuscript received 10 November 2016; published online 24 January 2017.

<sup>1</sup>The Pennsylvania State University, Department of Geosciences and Institute of Natural Gas Research, University Park, Pennsylvania, USA. E-mail: tyzhu@psu.edu.

<sup>2</sup>The University of Texas at Austin, Bureau of Economic Geology, John A. and Katherine G. Jackson School of Geosciences, Austin, Texas, USA. E-mail: junzhesun@utexas.edu.

© 2017 Society of Exploration Geophysicists. All rights reserved.

data sets (Zhou et al., 2011; Dutta and Schuster, 2014; Zhu and Harris, 2015). However, less attention has been given to the viscoelastic case. Deng and McMechan (2008) present a true-amplitude viscoelastic RTM algorithm, in which intrinsic attenuation is modeled by the generalized Zener model and memory variables (Carcione et al., 1988). Attenuation compensation is done by reversing the sign of the memory variable term in the viscoelastic wave equation. Nevertheless, as our earlier studies (Zhu, 2014, 2016; Zhu et al., 2014) explained, reversing the sign of the memory variable term describing coupled attenuation effects will not fully compensate for phase dispersion, which is numerically demonstrated in viscoacoustic media by Guo et al. (2016) and in viscoelastic media by Guo and McMechan (2015).

An alternative model is the frequency-independent  $Q$  (i.e., constant- $Q$ ) model proposed by Kjartansson (1979), which has been shown to appropriately describe the behavior of seismic waves in Pierre Shale (McDonald et al., 1958). Based on this model, Carcione (2009) derives the viscoelastic wave equation that involves a fractional time derivative, i.e., an irrational (or noninteger) order of the time derivative. Computing fractional time derivatives in the current time requires storing all previous time histories in memory and is not practical in seismic modeling studies, in particular, for 3D simulations. Zhu and Carcione (2014) derive the viscoelastic wave equation involving fractional space derivatives. This operator, computed with the fractional Fourier pseudospectral method, avoids the storage of wavefield histories, making the modeling as efficient as the simulation in elastic media. Using this wave equation, time reverse modeling can be implemented to reconstruct wavefields backward in time (Zhu, 2015a), which provides an efficient way to access the source wavefield in reverse time, while computing the adjoint field in RTM and full-waveform inversion (FWI) in viscoelastic media (Yang et al., 2016).

The goal of this paper is to present the theory of viscoelastic RTM based on such a time-domain viscoelastic wave equation and its

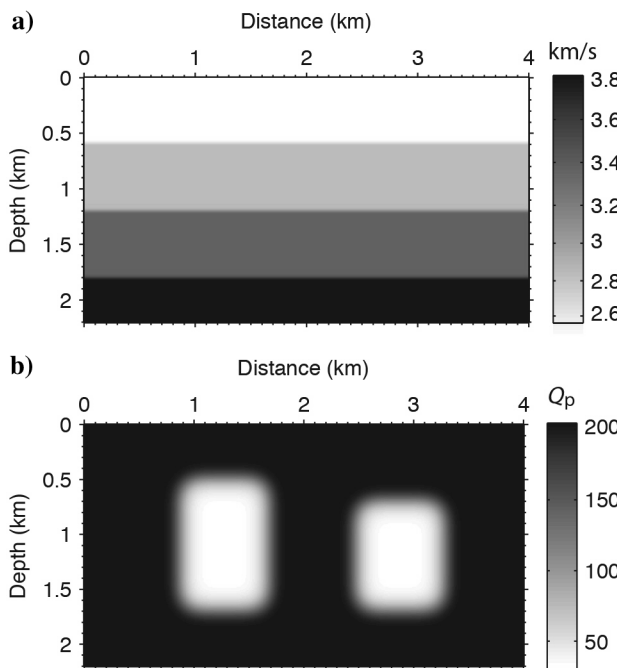


Figure 1. Velocity (a)  $V_p$  and (b)  $Q_p$  models.

back-propagation (time reverse) modeling. The key of the viscoelastic RTM algorithm is the compensation for P- and S-wave attenuation effects during wave extrapolation. This compensation relies on the decoupled P- and S-wave attenuation property in the viscoelastic wave equation (Zhu and Carcione, 2014). The first-order derivative terms in the wave equation correspond to P- and S-wave amplitude losses, and the remaining operators correspond to phase dispersion. We demonstrate this property using numerical simulations in a homogeneous model. We design a viscoelastic reverse time propagation approach that can correct for P- and S-attenuation effects, by reversing the sign of P- and S-amplitude loss operators. We note that, based on the same viscoelastic wave equation (Zhu and Carcione, 2014), Guo and McMechan (2015) develop a  $Q$ -compensated RTM method, and they find that  $Q$ -compensated RTM based on decoupled viscoelastic wave equation results in superior images compared with those produced by  $Q$ -compensated RTM based on nondecoupled (standard linear solid) viscoelastic wave equation.

The paper is organized as follows: We begin by using a synthetic model to illustrate the poor illumination problem caused by high attenuation zones when applying elastic RTM. Then, we formulate the theory of viscoelastic RTM by reviewing the viscoelastic wave equation, defining viscoelastic reverse time propagation with attenuation compensation, and describing the decomposed elastic imaging conditions in viscoelastic media. Finally, we demonstrate the effectiveness of viscoelastic RTM using 2D and 3D synthetic models.

## ELASTIC RTM IN THE PRESENCE OF ATTENUATION

In this section, we provide a demonstration of the illumination problem of elastic RTM using viscoelastic data. We do this by using a simple layered model with known viscoelastic attenuation, to investigate illumination problems in elastic RTM images caused by P- and S-waves attenuation.

We create a three-layer model with varying  $V_p$  and  $Q_p$  in Figure 1. The S-wave velocity  $V_s$  is calculated by  $V_s = V_p/1.7$ . A constant density ( $2200 \text{ kg/m}^3$ ) is chosen. In Figure 1b, there are two high attenuation zones ( $Q_p$  is approximately 30 and  $Q_s$  is approximately 20). The modeling grid is  $221 \times 401$  points. The grid spacings of the horizontal and vertical axes are  $\Delta x = \Delta z = 10 \text{ m}$ . A total of 41 sources are located at a depth of 70 m. The center frequency of the source wavelet is 25 Hz with a time delay of 0.04 s. The time step for modeling is 1.0 ms. The horizontal and vertical particle velocities are recorded with 400 receivers at a depth of 50 m. Synthetic seismic data, shown in Figure 2, are simulated by solving equations 1–5, and contain P- and S-wave attenuation effects.

We apply elastic RTM to the elastic data set to generate the reference images shown in Figure 3 and then to the viscoelastic data set. The P- and S-wave velocity models used for migration are obtained by smoothing the true models using a Gaussian filter. Figure 4 shows the PP- and PS-images, respectively. Some observations are as follows: below the 1.0 km depth, two reflectors in the PP-image appear in two shadow zones denoted by black arrows; in the PS-image, the top reflector exhibits weak energy focusing relative to PP-image and the bottom reflector is too weak to identify.

The poor illumination (i.e., shadow zones) is clearly caused by the high-attenuation zones that attenuate reflections traveling through

them. Migrating weak reflections would produce weak reflectors or even miss the reflectors in practice. For example, Li et al. (2007) observe that the PP-image missed the target structure due to a gas chimney above it. In the next section, we introduce a viscoelastic RTM algorithm to mitigate these attenuation effects and to improve image illumination.

## THEORY OF VISCOELASTIC RTM

The goal of viscoelastic RTM is to preserve accurate amplitude and phase information of the interfaces of the geologic structures. To achieve this goal, viscoelastic RTM needs to apply attenuation compensation during wave propagation, which is distinguished from elastic RTM (Yan and Sava, 2008). Our implementation of viscoelastic RTM consists of four steps: (1) forward propagation of the vector source wavefield by applying attenuation compensation, (2) reverse time propagation of seismic data to reconstruct the vector receiver wavefield by applying attenuation compensation, (3) decomposition of the vector source and receiver wavefields into P- and S-wave components, and (4) application of an imaging condition for the pure P- and S-wave modes. In this section, we explain in detail each of the steps in the processing flow. For simplicity, we show here all derivations in 2D. We provide the 3D velocity-stress formulation in Appendix A.

## Viscoelastic wave equation

First, we forward propagate seismic waves using a viscoelastic wave equation introduced by Zhu and Carcione (2014), where attenuation effect is quantified by the constant- $Q$  model (Kjartansson, 1979), i.e., frequency-independent  $Q$ . The 2D velocity-stress formulation of the viscoelastic wave equation in heterogeneous media is expressed as

$$\partial_t v_1 = \rho^{-1} (\partial_1 \sigma_{11} + \partial_3 \sigma_{13} + f_1), \quad (1)$$

$$\partial_t v_3 = \rho^{-1} (\partial_1 \sigma_{13} + \partial_3 \sigma_{33} + f_3), \quad (2)$$

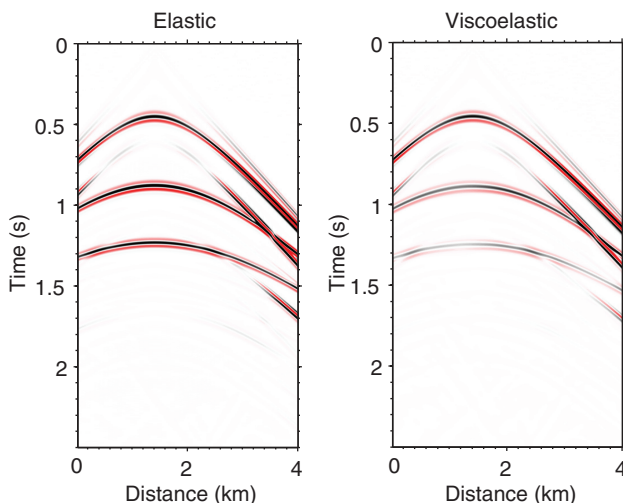


Figure 2. Synthetic shot gathers in (a) an elastic and (b) a viscoelastic medium.

$$\begin{aligned} \partial_t \sigma_{11} &= [\eta_p B_p (\partial_1 v_1 + \partial_3 v_3) - 2\eta_s B_s \partial_3 v_3] \\ &\quad + [\tau_p A_p \partial_t (\partial_1 v_1 + \partial_3 v_3) - 2\tau_s A_s \partial_t \partial_3 v_3], \end{aligned} \quad (3)$$

$$\begin{aligned} \partial_t \sigma_{33} &= [\eta_p B_p (\partial_1 v_1 + \partial_3 v_3) - 2\eta_s B_s \partial_1 v_1] \\ &\quad + [\tau_p A_p \partial_t (\partial_1 v_1 + \partial_3 v_3) - 2\tau_s A_s \partial_t \partial_1 v_1], \end{aligned} \quad (4)$$

$$\partial_t \sigma_{13} = [\eta_s B_s (\partial_3 v_1 + \partial_1 v_3) + \tau_s A_s \partial_t (\partial_3 v_1 + \partial_1 v_3)], \quad (5)$$

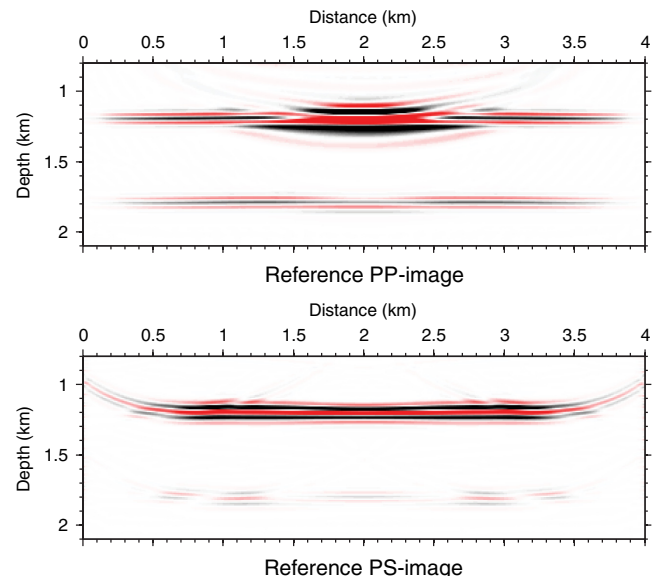


Figure 3. Reference elastic (a) PP- and (b) PS-images by applying elastic RTM on elastic data.

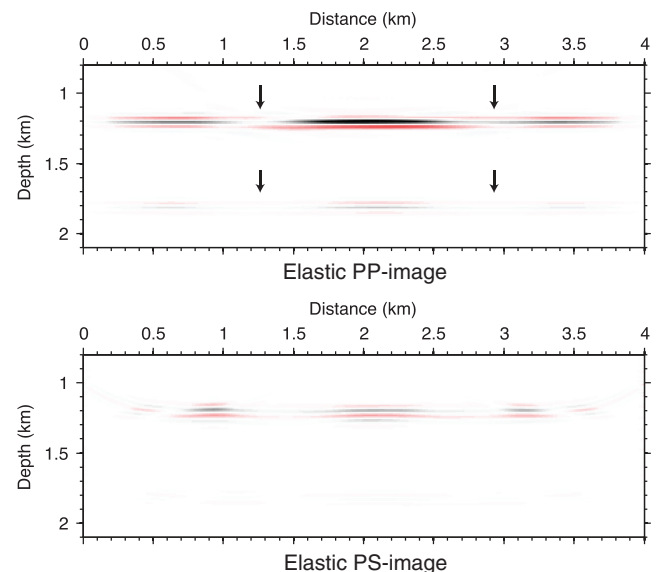


Figure 4. Elastic (a) PP- and (b) PS-images. Due to attenuation anomalies shown in Figure 1, both images appear the poor illumination of two reflectors with shadow zones indicated by arrows.

where  $\rho$  is the mass density;  $v_i$ ,  $\sigma_{ij}$ , and  $f_i$  denote the particle velocity, the stress, and body force components, respectively;  $i, j$  are the spatial indices; and

$$A_{P,S} = (-\nabla^2)^{\gamma_{P,S}-1/2}, B_{P,S} = (-\nabla^2)^{\gamma_{P,S}}, \quad (6)$$

where

$$\begin{aligned} \tau_P &= C_\lambda c_{P0}^{2\gamma_P-1} \sin(\pi\gamma_P), & \eta_P &= C_\lambda c_{P0}^{2\gamma_P} \cos(\pi\gamma_P), \\ \tau_S &= C_\mu c_{S0}^{2\gamma_S-1} \sin(\pi\gamma_S), & \eta_S &= C_\mu c_{S0}^{2\gamma_S} \cos(\pi\gamma_S), \\ C_\lambda &= M_0 \omega_0^{-2\gamma_P}, & C_\mu &= \mu_0 \omega_0^{-2\gamma_S}, \end{aligned} \quad (7)$$

and  $\omega_0$  is an arbitrary reference frequency that should be higher than the dominant source frequency to guarantee pulse delay with respect to the lossless case. In addition,  $\gamma_{P,S} = \arctan(Q_{P,S}^{-1})/\pi$ , and  $0 < \gamma_{P,S} < 0.5$  for any positive values of  $Q$ , where  $Q_p$  and  $Q_s$  are the P- and S-wave quality factors, respectively. The P-wave modulus  $M_0$  and the S-wave modulus  $\mu_0$  are given by  $M_0 = \rho c_{P0}^2 \cos^2(\arctan(Q_p^{-1})/2)$ , and  $\mu_0 = \rho c_{S0}^2 \cos^2(\arctan(Q_s^{-1})/2)$ , where  $c_{P0}$  and  $c_{S0}$  are the P- and S-wave velocities at the reference frequency, respectively.

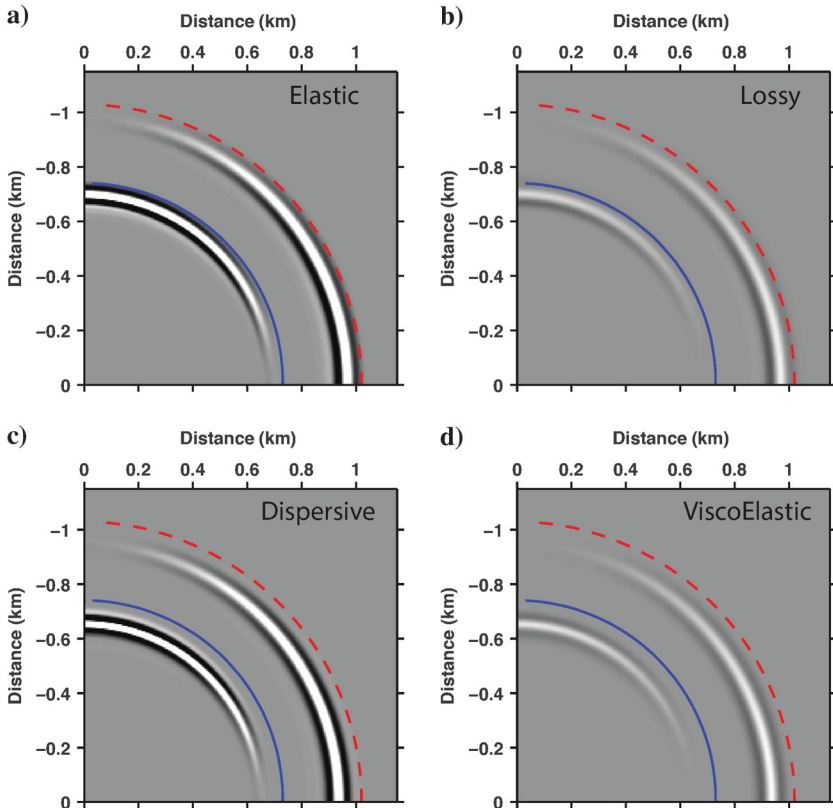


Figure 5. Wavefield snapshots using (a) elastic, (b) amplitude loss, (c) dispersive, and (d) viscoelastic. The elastic P-wavefront is labeled by the dashed red line, whereas the elastic S-wavefront is by the blue line. The P- and S-wavefronts are projected in all panels for comparisons of P- and S-wave phases.

Note that the first-order time-derivative terms (all  $A_{P,S}$  related terms) in equations 3–5 correspond to attenuation-associated P- and S-wave loss operators. When  $Q_{P,S} \rightarrow \infty$  ( $\gamma_{P,S} \rightarrow 0$ ), the first-order time-derivative terms disappear, and equations 1–5 only contain the second-order time derivatives, reducing to the classic elastic-wave equation.

To solve the wave equation in inhomogeneous media (equations 1–5), we use the staggered-grid finite-difference approach to discretize the time derivatives and the staggered-grid pseudospectral approach to discretize the first-order spatial derivatives. Recently, several numerical schemes have been proposed in geophysics to solve fractional Laplacian operators, for example, the Fourier-pseudospectral method (Carcione, 2010), the low-rank approximation (Sun et al., 2015), and the local method, namely, the Hermitian distributed approximation functional (Yao et al., 2017). In this study, we solve the fractional Laplacian operators using the Fourier pseudospectral method.

To demonstrate the decoupled amplitude loss and velocity dispersion for P- and S-waves, we build a homogeneous model with  $Q_p = 30$  and  $Q_s = 15$ . A vertical force source is put at the origin. Figure 5a shows the snapshot of the elastic simulation with  $Q_{P,S} \rightarrow \infty$ . The P-wavefront is indicated by the dashed red line, whereas the S-wavefront is indicated by the solid blue line. Figure 5b shows the amplitude-loss simulation (only weaker amplitude, no phase delay). Figure 5c shows the dispersion simulation (only phase delay, no amplitude loss).

It is worth noting that viscoelasticity should (physically) introduce phase delays in the waveform compared with the elastic case because a highly viscous medium tends to resist the wave propagation. Therefore, we prefer a high reference frequency as opposed to the low reference frequency often seen in the literature that advances the viscoelastic waveform over the elastic one. Figure 5d shows the viscoelastic simulation using equations 1–5 (weaker amplitude and phase delay). This decoupling property allows us to compensate for amplitude loss without compromising the phase accuracy in elastic images, which is explained in the next section.

### Viscoelastic reverse time propagation

Next, we reconstruct receiver wavefields by backward propagating recorded seismic data at the receiver locations. To implement backward propagation in the time-domain wave equation, we replace time  $t$  by  $-t$ . Note that, due to attenuation during forward propagation, the amplitude during back propagation of seismic data needs to be amplified. Here, the amplification of amplitude is done by reversing the sign of the P- and S-wave loss operators. Assuming  $\hat{t} = -t$ , the viscoelastic back-propagation modeling equations with attenuation compensation can be written as

$$\begin{aligned} \partial_t \hat{\sigma}_{11} &= [\eta_p B_p (\partial_1 \hat{v}_1 + \partial_3 \hat{v}_3) - 2\eta_s B_s \partial_3 \hat{v}_3] \\ &\quad - [\tau_p A_p \partial_t (\partial_1 \hat{v}_1 + \partial_3 \hat{v}_3) - 2\tau_s A_s \partial_t \partial_3 \hat{v}_3], \quad (8) \end{aligned}$$

$$\begin{aligned} \partial_t \hat{\sigma}_{33} = & [\eta_p B_p (\partial_1 \hat{v}_1 + \partial_3 \hat{v}_3) - 2\eta_s B_s \partial_1 \hat{v}_1] \\ & - [\tau_p A_p \partial_t (\partial_1 \hat{v}_1 + \partial_3 \hat{v}_3) - 2\tau_s A_s \partial_t \partial_1 \hat{v}_1], \end{aligned} \quad (9)$$

$$\partial_t \hat{\sigma}_{13} = \eta_s B_s (\partial_3 \hat{v}_1 + \partial_1 \hat{v}_3) - \tau_s A_s \partial_t (\partial_3 \hat{v}_1 + \partial_1 \hat{v}_3), \quad (10)$$

where  $\hat{\sigma}_{ij}$  and  $\hat{v}_i$  are the time-reversed variables. Combining equations 8–10 and equations 1 and 2 (with  $\hat{t} = -t$ ), we obtain the backward modeling equation to viscoelastic wave equation; i.e., the solution  $\hat{v}_i(\mathbf{x}, \hat{t}) = v_i(\mathbf{x}, -t)$  of equations 1, 2, 8, 9, and 10 is the time-reversed version of the solution  $v_i(\mathbf{x}, t)$  of the forward modeling equations 1–5, where  $\mathbf{x} = (x, y, z)$ . Because the wavefield ( $\hat{\sigma}_{ij}$ ) at a reversed time  $-t$  should agree exactly with that ( $\sigma_{ij}$ ) at a forward time  $t$ , the above system for time-reversal modeling becomes time invariant. This is why this viscoelastic wave equation is appropriate for time-reversal modeling with potential applications to least-squares (LS) imaging and FWI including viscoelasticity.

For the backward modeling, the input data consist of two particle velocity components (vertical  $d_3(\mathbf{x}_r, t)$  and horizontal  $d_1(\mathbf{x}_r, t)$ ) for 2D and three components for 3D. No body force is present during the time-reversal propagation; i.e.,  $f_i = 0$ . The recorded particle velocity components are reversed in time and enforced as the Dirichlet boundary condition at receivers; mathematically, this can be expressed as

$$\hat{v}_1(\mathbf{x}_r, -t) = d_1(\mathbf{x}_r, T - t), \quad (11)$$

$$\hat{v}_3(\mathbf{x}_r, -t) = d_3(\mathbf{x}_r, T - t), \quad (12)$$

where  $T$  is the total recording time and  $\mathbf{x}_r = (x_r, z_r)$  is the receiver location in 2D.

In practice, attenuation compensation during backward propagation may amplify not only signals but also some unwanted high-frequency noise. To prevent high-frequency noise from growing exponentially, we apply a low-pass filter in the spatial frequency domain to the right side amplitude loss and dispersion operators in equations 8–10 when back propagating the receiver wavefield. Note that the filter should be applied not to the full-propagation operators themselves but on P- and S-wave attenuation operators. Here, we show an importance of a low-pass filter during attenuation compensation using a homogeneous model. Full description of the simulation configuration can be found in the abstract (Zhu, 2015b). We ran attenuation compensation without applying a low-pass filter. Results are shown in Figure 6. Not surprisingly, without filtering, attenuation compensation will become unstable (black line). By applying a filter, remarkably, attenuation compensation can be stable and recover the amplitude and phase very well (yellow line) compared with the reference waveform (red line). A detailed description of how to choose such a filter is presented in Zhu (2016).

## Imaging condition

To apply the crosscorrelation imaging condition for multiple components of viscoelastic vector wavefields, we adopt the wavefield decomposition strategy described by Zhang and McMechan (2010), i.e., extract the pure wave modes (P and S) during extrapolation of the wavefield using a vector decomposition based on polarization. Two sequential vector (dot product) operations produce the decompositions of the vector P- and S-wavefields, respectively. For detailed implementations, we refer readers to check equations 15 and 17 in Zhang and McMechan (2010). As a result, the decomposed P-wavefield is a vector  $\{U_x^P, U_y^P, U_z^P\}$  as well as the vector S-wavefield  $\{U_x^S, U_y^S, U_z^S\}$ , where the symbols P and S

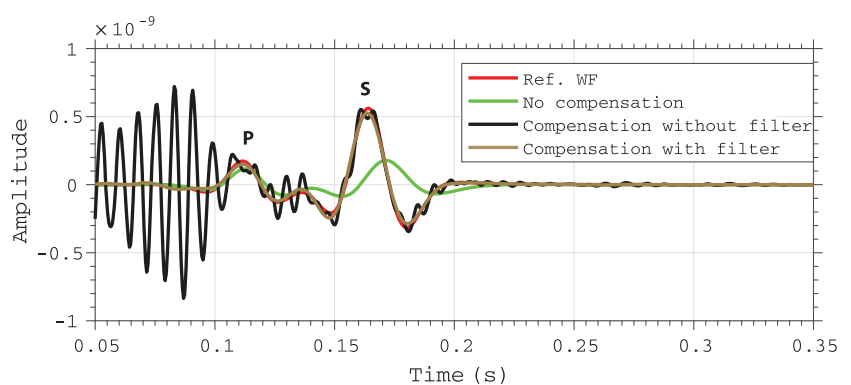


Figure 6. Waveforms (horizontal particle velocity component) recorded at the reference point A indicated in Figure 2 in the abstract (Zhu, 2015b). Red: waveform recorded in the forward simulation using viscoelastic forward modeling. Green: waveform reconstructed by elastic back propagation. Black: waveform reconstructed by attenuation compensation viscoelastic back propagation without applying a low-pass filter. Yellow: waveform reconstructed by attenuation compensation viscoelastic back propagation with applying a low-pass filter. Labels P and S denote P- and S-waves, respectively.

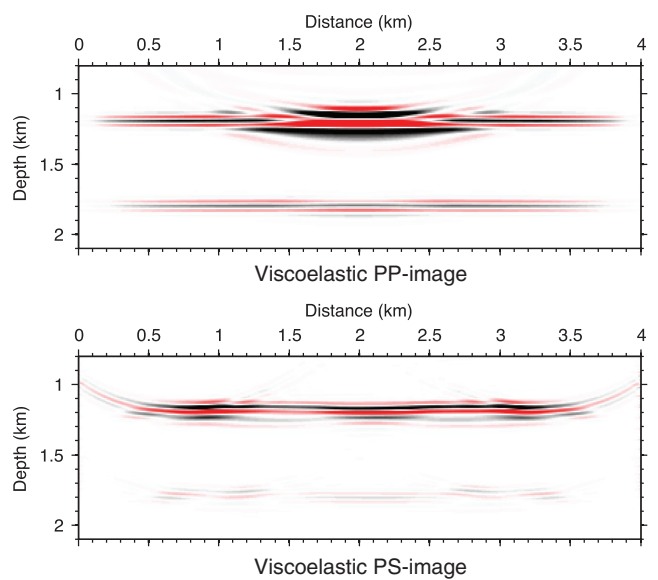


Figure 7. Viscoelastic (a) PP- and (b) PS-images. Compared with elastic images in Figure 4, the shadow zones are illuminated.

represent compressional and transverse components of the wavefield, respectively,

Using the decomposed P- and S-components, we can formulate a PP-imaging condition that produces an image by applying the dot product of the P-wave components of the source and receiver wavefields (Wang et al., 2015)

$$I_{PP}(\mathbf{x}) = \int \mathbf{S}_P^C(\mathbf{x}, t) \cdot \mathbf{R}_P^C(\mathbf{x}, t) dt, \quad (13)$$

and, similarly, a PS-imaging condition that produces an image by applying the dot product of the P-wave mode of the source wavefield and the S-wave mode of the receiver wavefield (Wang et al., 2015)

$$I_{PS}(\mathbf{x}) = \int \mathbf{S}_P^C(\mathbf{x}, t) \cdot \mathbf{R}_S^C(\mathbf{x}, t) dt, \quad (14)$$

where the symbols  $\mathbf{S}$  and  $\mathbf{R}$  stand for the vector source and receiver wavefields, respectively, the subscripts  $\{P, S\}$  represent the various

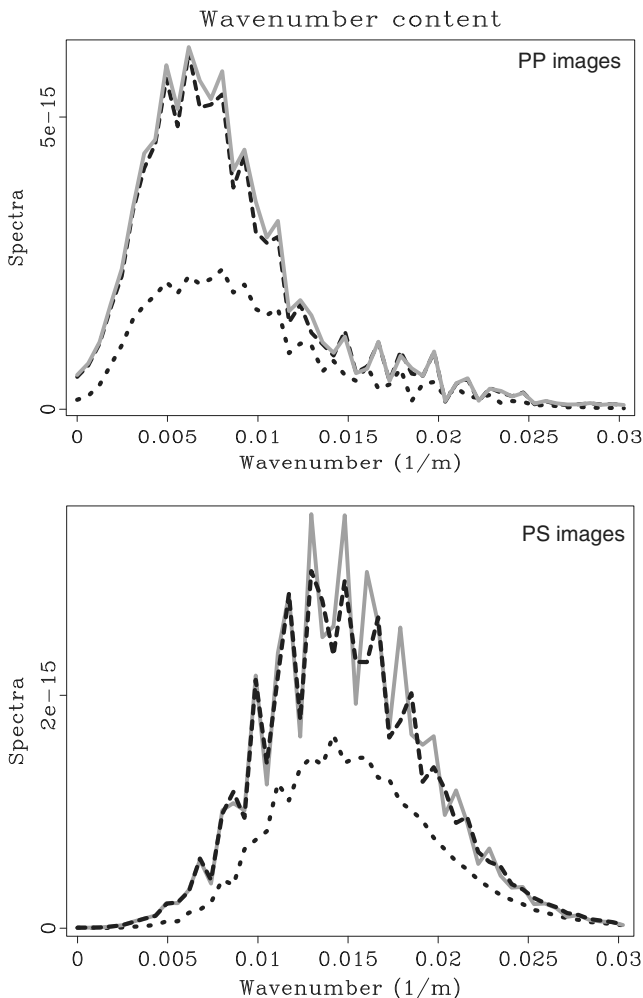


Figure 8. Wavenumber content of (a) PP- and (b) PS-images in Figure 7. Dotted line: elastic images without attenuation compensation. Dashed line: viscoelastic images with attenuation compensation. Solid line: reference.

pure P- and S-wave modes of the wavefields, and the superscript "C" refers to attenuation compensation. Similarly, this imaging condition results in other types of seismic images, e.g.,  $I_{SP}$  and  $I_{SS}$ . Note that if the deconvolution imaging condition instead of cross-correlation is used, attenuation compensation should be applied to backward wave propagation (step 2) only but not to forward propagation (step 1) (Zhu, 2016).

In the previous section, we show the poor illumination problem of elastic RTM images. Here, we apply the above viscoelastic RTM algorithm to the same model to demonstrate the benefits of viscoelastic RTM. Figure 7 shows the PP- and PS-images using viscoelastic RTM. In contrast to the PP- and PS-images obtained using elastic RTM in Figure 4, Figure 7 clearly shows improved PP- and PS-images with better illumination of the second and third

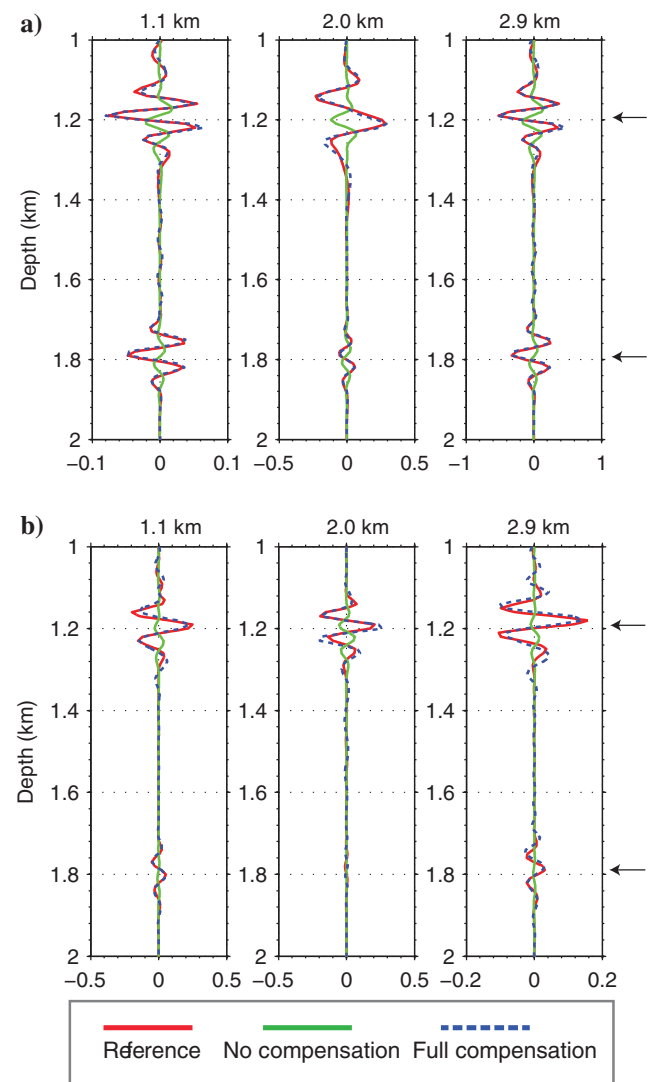


Figure 9. Comparisons of three traces of the (a) PP- and (b) PS-images between the reference (Figure 3), the elastic image (Figure 4), and the full compensated image (Figure 7). The reference trace is marked by the solid red line, the trace without compensation is marked by the green line, and the dashed blue line indicates the compensated trace. The image traces are selected at the horizontal offset of 1.1, 2.0, and 2.9 km. Arrows point to the reflector.

reflectors. The shadow zones are clearly illuminated in the PP- and PS-images. Figure 8 compares the wavenumber content of elastic, viscoelastic, and reference PP-and PS-images. Viscoelastic PP- and PS-images using viscoelastic RTM contain high wavenumbers close to the reference ones.

We now compare image traces at different offsets (1.1, 2.0, and 2.9 km) to verify that the reflection events are migrated to the correct depth level. Figure 9a shows a comparison of three traces from the PP-image. Remarkably, the compensated traces (dashed blue lines) from the PP-images show excellent agreement with the reference one (solid red lines) in amplitude and phase. Comparison of the PS-image traces in Figure 9b also shows that the compensated traces (dashed blue lines) closely match with the reference ones (solid red lines).

As shown in the PS-images, the bottom reflector is weak and discontinuous, which may be caused by the imaging condition, i.e., the dot product without accounting for the angle between the vector wavefields. This problem could be reconciled by exploring better

imaging conditions, for example, using an angle-domain imaging condition (Yan and Xie, 2012; Wang et al., 2016) or a scalar imaging condition following Helmholtz decomposition (Duan and Sava, 2015). We also apply phase-only compensation by setting amplitude terms to be zeros to migrate the viscoelastic data. A comparison of the details is shown in Figure 10. Not surprisingly, phase-only compensated traces (gray) exhibit a better match to the reference traces (red) in phase, whereas their amplitudes are similar to the traces without compensation (green).

In summary, with attenuation compensation, compensated PP- and PS-images show improved illumination of reflectors with corrected amplitude and phase. This result is very encouraging for further practical applications.

## SYNTHETIC EXAMPLES

In this section, we evaluate the proposed viscoelastic RTM algorithm using 2D and 3D synthetic models. Because a  $Q_s$  model is

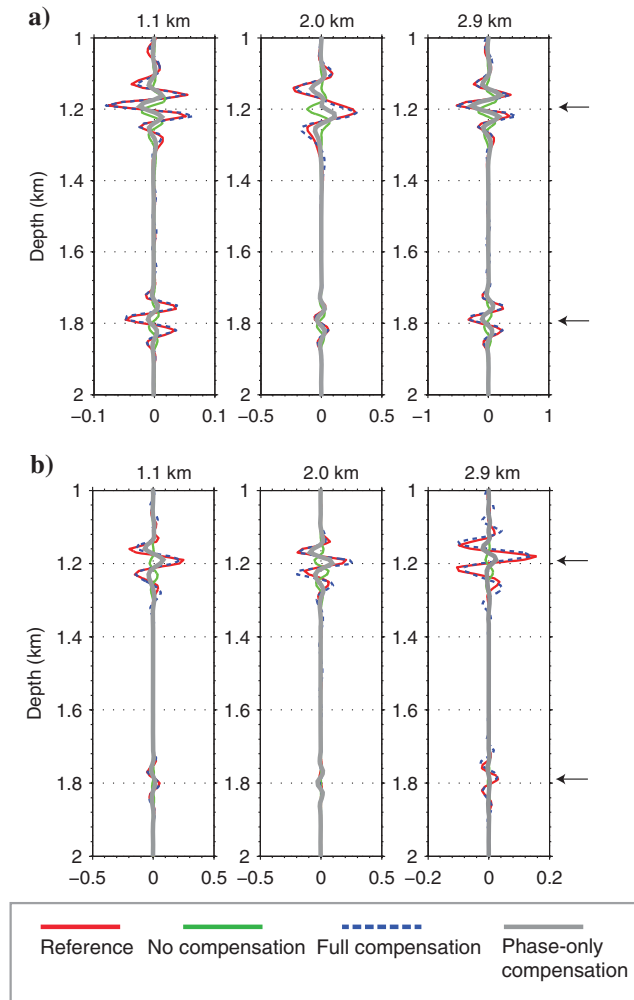


Figure 10. The gray traces by using the phase-only compensation overlaying in Figure 9. It is clear that the phase dispersion is corrected, whereas the amplitude is similar to no-compensation ones (green).

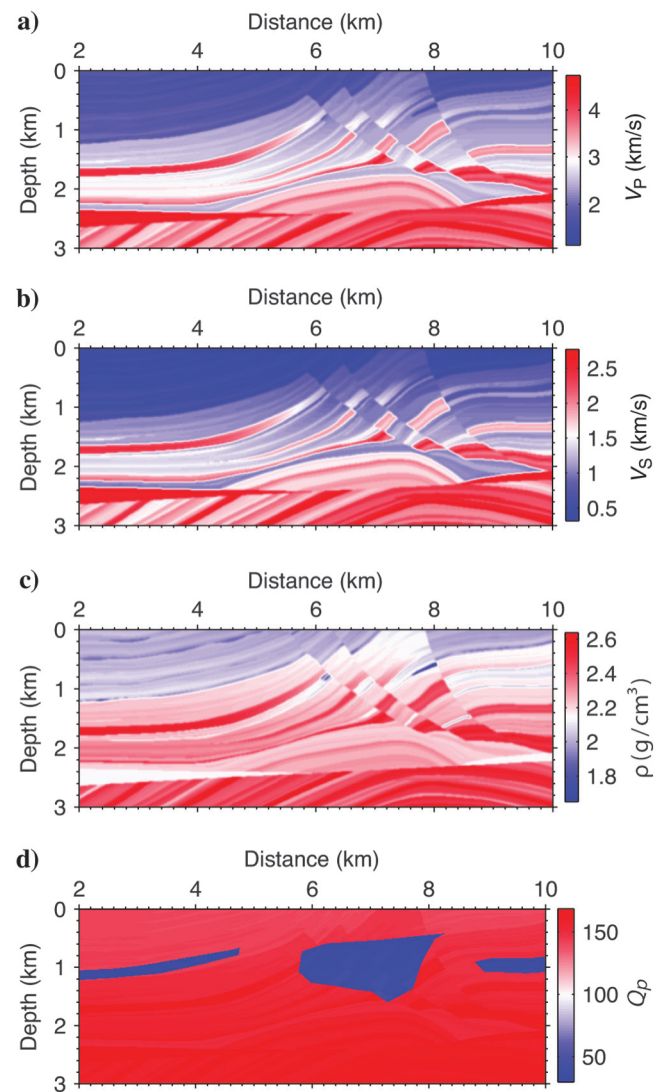


Figure 11. Marmousi seismic models. They are (a)  $V_p$ , (b)  $V_s$ , (c) density  $\rho$ , and (d)  $Q_p$ .

usually not available, we let  $Q_s = Q_p$  in all examples. Synthetic data sets are generated by solving the viscoelastic wave equation (equations 1–5). For the 2D examples, explosive sources are used, and a perfectly matched layer absorbing boundary (Berenger, 1994) with the thickness of 20 grid spacings at the four sides is used to eliminate edge reflections. For the 3D example, we solve the velocity-stress viscoelastic wave equation (see Appendix A) and we use a combination of one-way absorbing boundary layers and sponge layers to eliminate edge reflections. Smoothed P- and S-wave velocity models are used for RTM, and the true  $Q_p$  and  $Q_s$  models are used for viscoelastic RTM. A Laplacian filter is applied to all the RTM images for the suppression of low-wavenumber noise (Zhang and Sun, 2009). To stabilize viscoelastic RTM when amplifying the signals, we choose a Tukey low-pass filter with a cutoff frequency of 100 Hz and a taper ratio of 0.2 to suppress the noise growth.

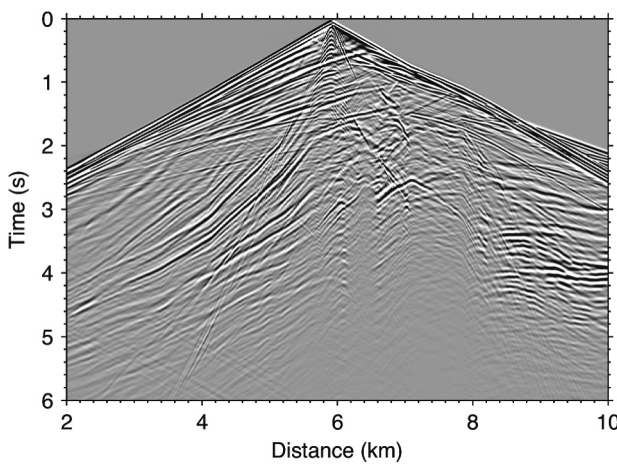


Figure 12. Shot gather synthetic data by viscoelastic forward modeling.

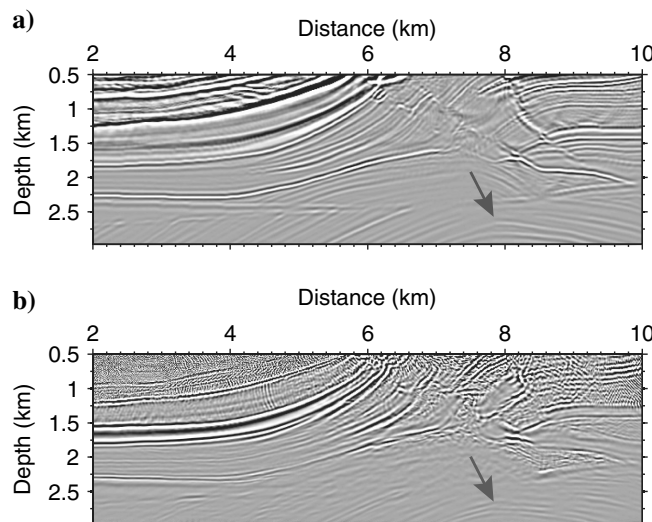


Figure 13. (a) The PP- and (b) PS-images by elastic RTM. The deep area indicated by an arrow shows poor illumination caused by the upper attenuation areas. (c) The PP- and (d) PS-images by viscoelastic RTM. Remarkably, the deep area shows better illumination in the PP- and PS-images than (a and c).

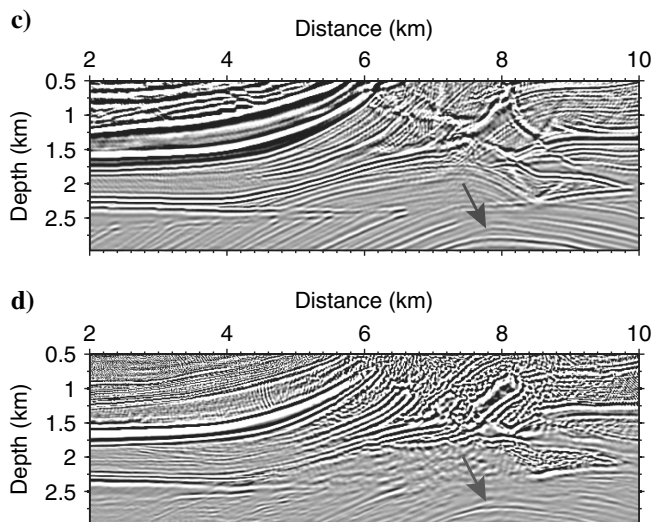
## Marmousi-2 model

In the first example, we choose the Marmousi-2 elastic model without the shallow water layer (Martin et al., 2006). Three high-attenuation zones are embedded within a shallow sedimentary section, which contains several faults, an unconformity, and a hydrocarbon reservoir at the bottom (Figure 11). Three high-attenuation zones attenuate reflections from the area deeper below, and result in seriously poor illumination of the deep structure, especially the center part with the strongest attenuation body, when conventional elastic RTM is used.

The model is discretized with grid points of  $281 \times 1001$ . The grid spacing on the horizontal and vertical axes is  $\Delta x = \Delta z = 12.5$  m. There are 120 sources, with each source being a Ricker wavelet with a center frequency of 20 Hz. The shot interval is 125 m, whereas the receiver spacing is 12.5 m with a total of 959 receivers. Sources and receivers are located at a depth of 62.5 m. The seismograms are recorded for a total time of 6.0 s, and the sampling rate is 1.0 ms. Viscoelastic synthetic data sets are calculated using a forward-modeling scheme using equations 1–5. A modeled shot gather is shown in Figure 12.

Again, we first perform the elastic RTM. Figure 13a shows the resulting PP-image with limited structural features, e.g., sediments and faults. In the deeper part, the amplitude overall is relatively weaker, especially the anticline structure beneath the high attenuation zone (below a depth of 1.5 km). The anticline structures around the depth of 2.0 km disappear. The hydrocarbon reservoir is not adequately delineated. Similarly, the PS image in Figure 13b presents an informative characterization of the shallow sediments, but it is dimmed in the deeper area. Again, the important hydrocarbon reservoirs are not imaged. It is not surprising that elastic RTM images fail to provide a detailed structural image of the deep area beneath the attenuation zones.

To mitigate attenuation effects and improve the image quality, viscoelastic RTM is applied to the synthetic data. Figure 13c and 13d shows the  $Q$ -compensated PP- and PS-images. Clearly, the



compensated images overall show a properly recovered amplitude, especially in the deeper area. The sediments and interfaces are imaged to be continuous, for example, the sediments below the gas charged sand channel (0.5 km). Magnified views of this part are shown in Figure 14c and 14d. The reflectors at approximately 1.6 and 1.8 km are clearly enhanced. At approximately 2.3 km, com-

pared with Figure 14a and 14b, an unconformity structure feature is delineated in Figure 14c and 14d. In addition, the top of the anticline below 1.5 km in the central part of the model appears to be better illuminated with more details. A magnified view of this part is shown in Figure 15c and 15d. The hydrocarbon reservoirs are imaged in PP- and PS-images, as indicated by the arrows. In this case,

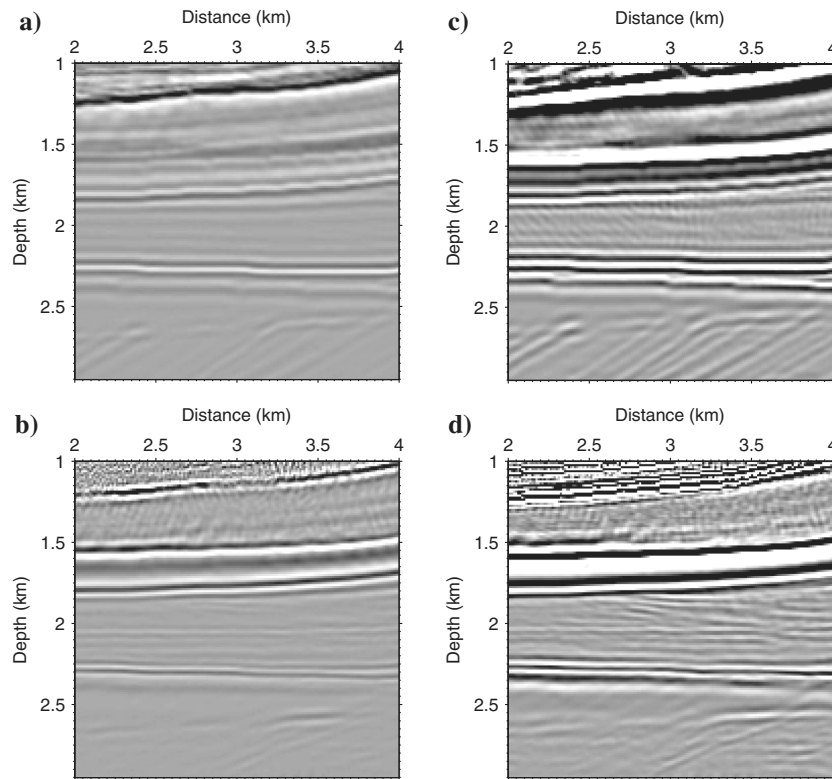


Figure 14. Magnified view of the left section of the (a) PP- and (b) PS-images in Figure 13.

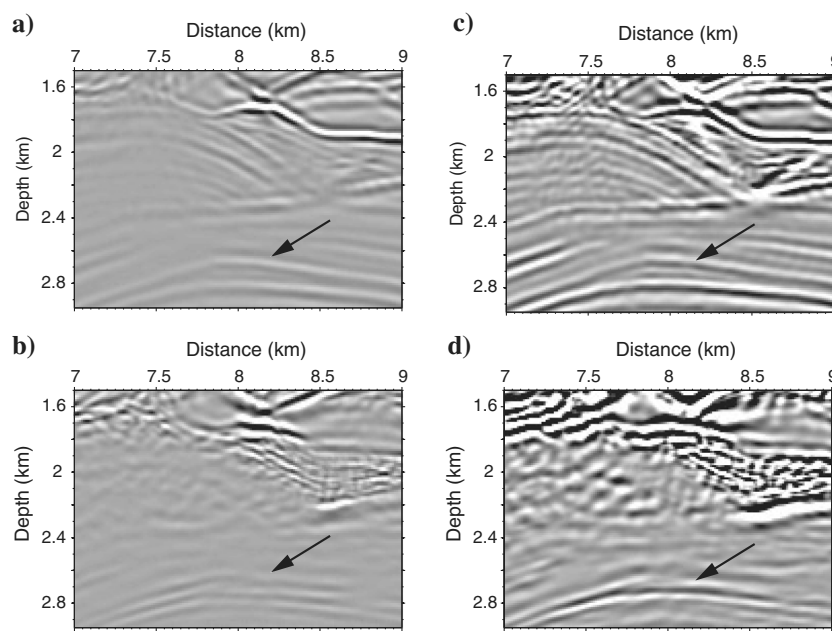


Figure 15. Magnified view of the middle section of the (a) PP- and (b) PS-images in Figure 13.

viscoelastic RTM successfully improved the image quality by revealing geologic features that are not well-imaged or are nearly invisible using elastic RTM.

We also test our approach with noisy data by adding Gaussian random noise to the viscoelastic data, where the S/N = 10 dB (see Figure 16a). Figure 16b and 16c shows the results of PP- and PS-images. Compared with results with noise-free data, PP- and PS-images become slightly noisier but still preserve the geologic structures (e.g., the anticline at the depth of 2.8 km) as expected.

### 3D model

In the last example, we present 3D imaging results of a small portion of the 3D SEAM model (Fehler and Kelih, 2011). Figure 17a and 17b shows the P-wave velocity and  $Q_p$  models, respectively. The S-wave velocity  $V_S$  is calculated by  $V_S = V_P/1.43$ . The density is assumed to be constant with  $\rho = 2000 \text{ kg/m}^3$ . The model is discretized with a grid of  $100 \times 100 \times 100$ . The grid spacings for  $x$ ,  $y$ , and  $z$  are 20 m. The time step length is 1 ms. We deploy 16 explosive sources at a depth of 20 m. A 20 Hz Ricker wavelet is used as the source. Figure 18a and 18b shows two modeled shot gathers (horizontal  $x$ -component) without  $Q$ -effects (elastic) and with  $Q$ -effects (viscoelastic), respectively. In the later part, seismic reflections and diffractions are attenuated and time delayed compared with the elastic case.

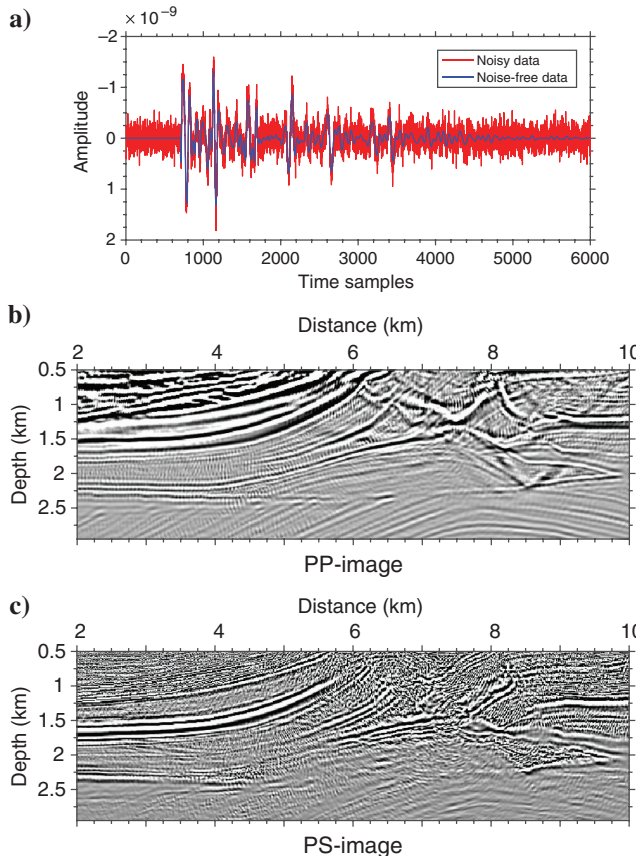


Figure 16. Applying viscoelastic RTM on noisy data. (a) Shows a noisy trace and a noise-free trace at the location of 5 km from Figure 12, as well as (b) PP- and (c) PS-images.

We apply elastic and viscoelastic RTM imaging to viscoelastic seismic data. Figures 19a and 20a show elastic PP- and PS-images, respectively. Figures 19b and 20b show viscoelastic PP- and PS-images. Without compensation, salt flanks in the image are shifted down relative to the reference depth. Salt boundaries appear dimmed. With  $Q$ -compensation, the salt flanks labeled by arrows are better imaged at the correct depth compared with the reference images (Figures 19c and 20c). The boundaries of the salt body are fairly enhanced (see the top-right panel) and shifted back to the correct locations.

### DISCUSSION

The success of viscoelastic RTM relies on two properties of the fundamental viscoelastic wave equation: (1) either amplitude loss or velocity dispersion can be independently modeled during wave propagation and (2) the back propagation equation is formulated by reversing the sign of P- and S-wave loss operators, which simultaneously compensates for the P- and S-wave attenuation effects in the reconstructed wavefield. The major concern on attenuation

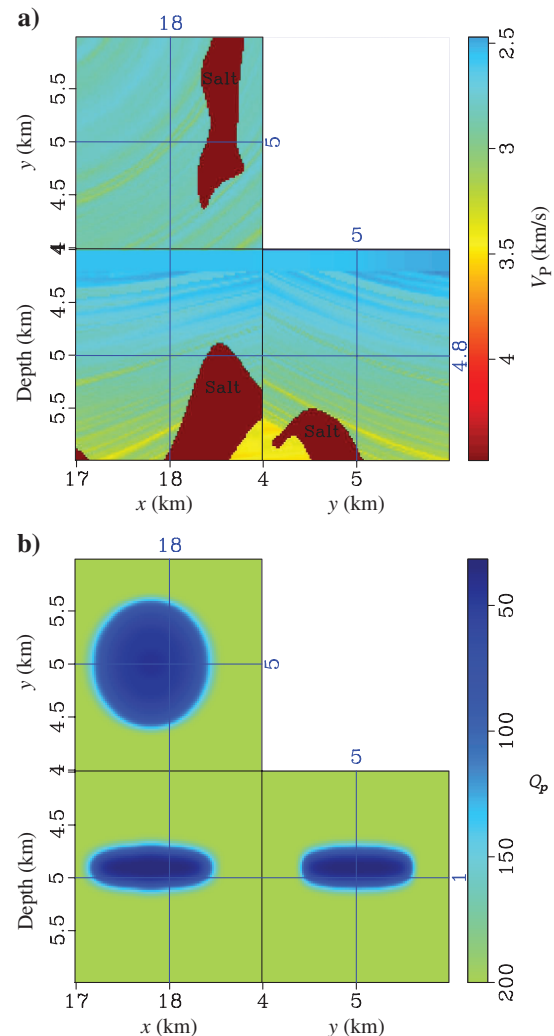


Figure 17. The P-wave velocity (a)  $V_P$  model from SEAM and (b)  $Q_p$  models.

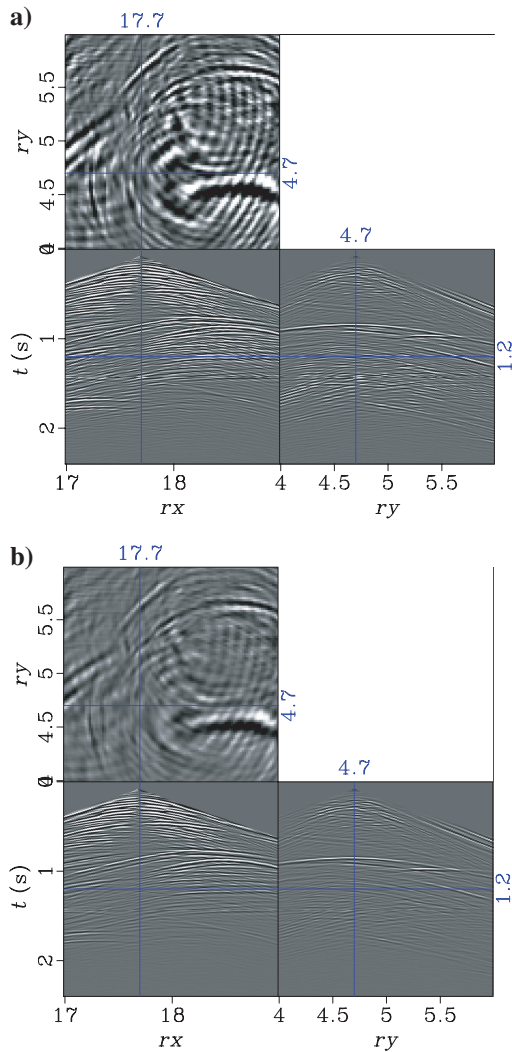


Figure 18. Horizontal component of the (a) elastic data and (b) viscoelastic data. Attenuation effects can be clearly observed in the viscoelastic data. Here,  $rx$  and  $ry$  are in km.

compensation is the stability of wave propagation when the amplitude is amplified; i.e., more high-frequencies are recovered. In our experience, numerical stability can be guaranteed by applying strict low-pass filters on the amplitude compensation operator, which may compromise the image resolution. On the other hand, our recent work has shown that smooth division between a phase-only wavefield and a viscoacoustic wavefield can be used to create a stable attenuation compensation operator without explicitly amplifying the wave amplitude (Sun and Zhu, 2015). This strategy can be straightforwardly adopted in viscoelastic RTM.

The proposed methodology can find applications in FWI in attenuating media. For instance, the most intuitive strategy is to store the source wavefield when performing the forward modeling and access it at each time step when computing the adjoint wavefield for building the gradient. For large-scale 3D FWI applications, however, the wavefield storage approach is infeasible for memory and inefficient for disk. Instead of storing the source wavefield, reverse time propagation with appropriate compensation can reconstruct the source wavefield from the saved boundaries. Yang et al. (2016) demonstrate by numerical experiments that using the reconstructed source wavefield and the computed adjoint wavefield at each time step can build FWI gradients with adequate accuracy in attenuating media. Applications of  $Q$ -compensation in LSRTM proposed by Sun et al. (2016) improve the convergence rate of LSRTM in viscoacoustic media. They show that the wave equation Hessian can be preconditioned by replacing the adjoint operator by  $Q$ -compensated RTM. Later, Xue et al. (2016) present an application of  $Q$ -compensation in viscoacoustic FWI. They construct a  $Q$ -compensated gradient, which has the recovered amplitude while preserving the correct kinematics. They show that using the  $Q$ -compensated gradient can lead to faster convergence of the FWI process.

We anticipate that independent compensation for phase and amplitude may also provide a strategy for separately updating the velocity and attenuation in FWI. One can invert for only elastic velocity while fixing attenuation as a first step to match the phase information using the dispersion-only wave equation and then invert for attenuation to fit the rest of the residual phase and amplitudes of seismic data using the full viscoelastic wave equation. To fully match the amplitudes, density has to be taken into consideration.

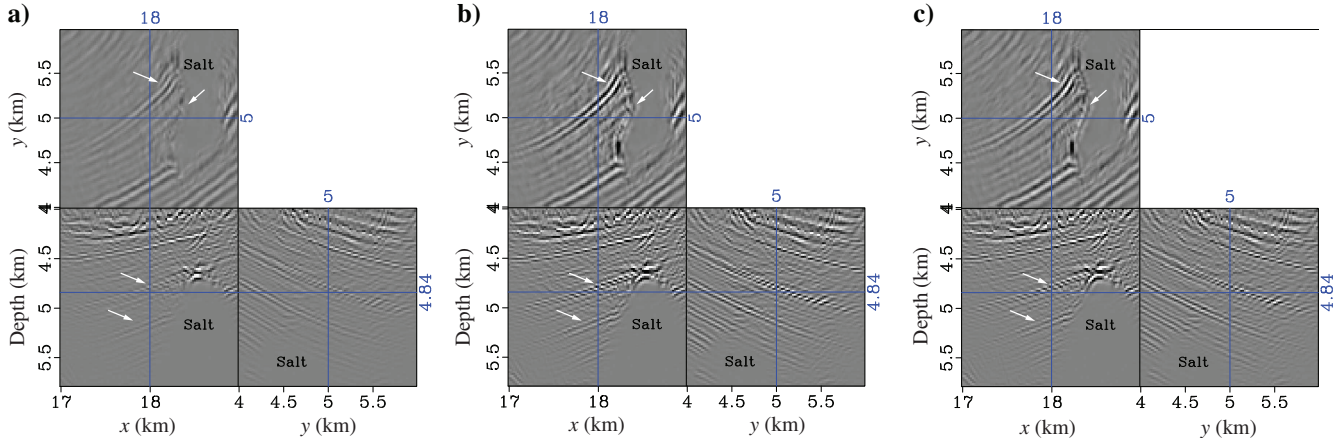


Figure 19. (a) The PP-image by elastic RTM. Salt flanks under the high-attenuation zone are poorly illuminated, and the salt boundaries are not well-delineated. (b) The PP-image by viscoelastic RTM. Remarkably, the salt flanks and boundaries labeled by the arrows show better illumination than (a). (c) The reference PP-image.

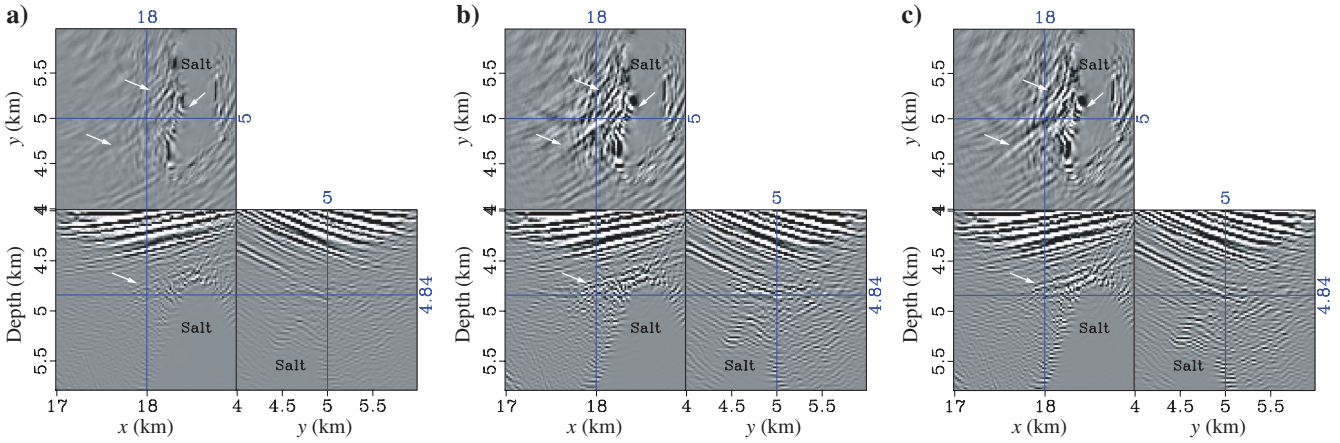


Figure 20. (a) The PS-image by elastic RTM. (b) The PS-image by viscoelastic RTM. (c) The reference PS-image. Compared with (a), (b) shows many improvements of salt flanks and boundaries labeled by white arrows.

## CONCLUSION

We have presented a viscoelastic RTM imaging algorithm based on a decoupled viscoelastic wave equation. The decoupled wave equation provides a simple way to perform P- and S-wave attenuation compensation during wave propagation. Synthetic examples have shown that it is possible to compensate for P- and S-wave attenuation effects including amplitude loss and phase dispersion. We also showed that either amplitude loss or phase dispersion can be mitigated independently using the corresponding wave equation. With an appropriate low-pass filter, attenuation compensation is robust to noisy data (e.g., S/N = 10 dB). Viscoelastic RTM of multicomponent data can be a powerful tool that provides a high-resolution and amplitude-balanced illumination of target structures, particularly beneath high-attenuation areas, which are not well-imaged or are nearly invisible using elastic RTM.

## ACKNOWLEDGMENTS

We acknowledge J. Schleicher, A. Stanton, G. Dutta, and one anonymous reviewers for their critical comments that significantly improved the manuscript. We also thank S. Fomel for reading the first draft and J. Cheng (Tongji University) for discussions on wave-field decomposition. T. Zhu was supported by the startup funding from the Department of Geosciences and Institute of Natural Gas Research at the Pennsylvania State University. Much of this study was done when T. Zhu was a postdoc fellow at the University of Texas at Austin supported by Jackson Postdoctoral Fellowship. J. Sun was supported by a Statoil Fellowship at the University of Texas at Austin.

## APPENDIX A

### 3D VISCOELASTIC WAVE EQUATION

The 3D velocity-stress formulation of the viscoelastic wave equation can be expressed as

$$\rho \partial_t v_1 = \partial_1 \sigma_{11} + \partial_2 \sigma_{12} + \partial_3 \sigma_{13} + f_1, \quad (\text{A-1})$$

$$\rho \partial_t v_2 = \partial_1 \sigma_{12} + \partial_2 \sigma_{22} + \partial_3 \sigma_{23} + f_2, \quad (\text{A-2})$$

$$\rho \partial_t v_3 = \partial_1 \sigma_{13} + \partial_2 \sigma_{23} + \partial_3 \sigma_{33} + f_3, \quad (\text{A-3})$$

$$\begin{aligned} \partial_t \sigma_{11} = & [\eta_p B_p (\partial_1 v_1 + \partial_2 v_2 + \partial_3 v_3) - 2\eta_s B_s (\partial_2 v_2 + \partial_3 v_3)] \\ & + [\tau_p A_p \partial_t (\partial_1 v_1 + \partial_2 v_2 + \partial_3 v_3) - 2\tau_s A_s \partial_t (\partial_2 v_2 + \partial_3 v_3)], \end{aligned} \quad (\text{A-4})$$

$$\begin{aligned} \partial_t \sigma_{22} = & [\eta_p B_p (\partial_1 v_1 + \partial_2 v_2 + \partial_3 v_3) - 2\eta_s B_s (\partial_1 v_1 + \partial_3 v_3)] \\ & + [\tau_p A_p \partial_t (\partial_1 v_1 + \partial_2 v_2 + \partial_3 v_3) - 2\tau_s A_s \partial_t (\partial_1 v_1 + \partial_3 v_3)], \end{aligned} \quad (\text{A-5})$$

$$\begin{aligned} \partial_t \sigma_{33} = & [\eta_p B_p (\partial_1 v_1 + \partial_2 v_2 + \partial_3 v_3) - 2\eta_s B_s (\partial_1 v_1 + \partial_2 v_2)] \\ & + [\tau_p A_p \partial_t (\partial_1 v_1 + \partial_2 v_2 + \partial_3 v_3) - 2\tau_s A_s \partial_t (\partial_1 v_1 + \partial_2 v_2)], \end{aligned} \quad (\text{A-6})$$

$$\partial_t \sigma_{12} = [\eta_s B_s (\partial_2 v_1 + \partial_1 v_2) + \tau_s A_s \partial_t (\partial_2 v_1 + \partial_1 v_2)], \quad (\text{A-7})$$

$$\partial_t \sigma_{13} = [\eta_s B_s (\partial_3 v_1 + \partial_1 v_3) + \tau_s A_s \partial_t (\partial_3 v_1 + \partial_1 v_3)], \quad (\text{A-8})$$

$$\partial_t \sigma_{23} = [\eta_s B_s (\partial_3 v_2 + \partial_2 v_3) + \tau_s A_s \partial_t (\partial_3 v_2 + \partial_2 v_3)], \quad (\text{A-9})$$

where

$$A_{P,S} = (-\nabla^2)^{\gamma_{P,S}-1/2}, B_{P,S} = (-\nabla^2)^{\gamma_{P,S}}. \quad (\text{A-10})$$

Here, all variables are defined in the context of the “Viscoelastic wave equation” section. The backward equation for attenuation compensation is obtained by reversing the sign of the first time derivative terms, which makes the equations time invariant for time-reverse modeling.

## REFERENCES

- Berenger, J., 1994, A perfectly matched layer for the absorption of electromagnetic waves: *Journal of Computational Physics*, **114**, 185–200, doi: [10.1006/jcph.1994.1159](https://doi.org/10.1006/jcph.1994.1159).
- Browaeys, T. J., and S. Fomel, 2009, Fractal heterogeneities in sonic logs and low-frequency scattering attenuation: *Geophysics*, **74**, no. 2, WA77–WA92, doi: [10.1190/1.3062859](https://doi.org/10.1190/1.3062859).
- Carcione, J. M., 2009, Theory and modeling of constant-*Q* P- and S-waves using fractional time derivatives: *Geophysics*, **74**, no. 1, T1–T11, doi: [10.1190/1.3008548](https://doi.org/10.1190/1.3008548).
- Carcione, J. M., 2010, A generalization of the Fourier pseudospectral method: *Geophysics*, **75**, no. 6, A53–A56, doi: [10.1190/1.3509472](https://doi.org/10.1190/1.3509472).
- Carcione, J. M., D. Kosloff, and R. Kosloff, 1988, Wave propagation simulation in a linear viscoelastic medium: *Geophysical Journal*, **95**, 597–611, doi: [10.1111/j.1365-246X.1988.tb06706.x](https://doi.org/10.1111/j.1365-246X.1988.tb06706.x).
- Chang, W., and G. A. McMechan, 1987, Elastic reverse time migration: *Geophysics*, **52**, 1365–1375, doi: [10.1190/1.1442249](https://doi.org/10.1190/1.1442249).
- Deng, F., and G. McMechan, 2007, True-amplitude prestack depth migration: *Geophysics*, **72**, no. 3, S155–S166, doi: [10.1190/1.2714334](https://doi.org/10.1190/1.2714334).
- Deng, F., and G. McMechan, 2008, Viscoelastic true-amplitude prestack reverse-time depth migration: *Geophysics*, **73**, no. 4, S143–S155, doi: [10.1190/1.2938083](https://doi.org/10.1190/1.2938083).
- Duan, Y., and P. Sava, 2015, Scalar imaging condition for elastic reverse time migration: *Geophysics*, **80**, no. 4, S127–S136, doi: [10.1190/geo2014-0453.1](https://doi.org/10.1190/geo2014-0453.1).
- Dutta, G., and G. T. Schuster, 2014, Attenuation compensation for least-squares reverse time migration using the viscoacoustic-wave equation: *Geophysics*, **79**, no. 6, S251–S262, doi: [10.1190/geo2013-0414.1](https://doi.org/10.1190/geo2013-0414.1).
- Fehler, M., and P. Keliher, 2011, SEAM phase 1: Challenges of subsalt imaging in tertiary basins, with emphasis on deepwater Gulf of Mexico: SEG.
- Fletcher, R., D. Nichols, and M. Cavalca, 2012, Wavepath-consistent effective *Q* estimation for *Q*-compensated reverse-time migration: 74th Annual International Conference and Exhibition, EAGE, Extended Abstracts, doi: [10.3997/2214-4609.20148360](https://doi.org/10.3997/2214-4609.20148360).
- Guo, P., and G. A. McMechan, 2015, Separation of absorption and dispersion effects in *Q*-compensated viscoelastic RTM: 85th Annual International Meeting, SEG, Expanded Abstracts, 3966–3971.
- Guo, P., G. A. McMechan, and H. Guan, 2016, Comparison of two viscoacoustic propagators for *Q*-compensated reverse time migration: *Geophysics*, **81**, no. 5, S281–S297, doi: [10.1190/geo2015-0557.1](https://doi.org/10.1190/geo2015-0557.1).
- Hardage, B., M. DeAngelo, P. Murray, and D. Sava, 2011, Multicomponent seismic technology: SEG.
- Hokstad, K., 2000, Multicomponent Kirchhoff migration: *Geophysics*, **65**, 861–873, doi: [10.1190/1.1444783](https://doi.org/10.1190/1.1444783).
- Kjartansson, E., 1979, Constant-*Q* wave propagation and attenuation: *Journal of Geophysical Research*, **84**, 4737–4748, doi: [10.1029/JB084B09p04737](https://doi.org/10.1029/JB084B09p04737).
- Klimontos, T., 1995, Attenuation of P and S-waves as a method of distinguishing gas and condensate from oil and water: *Geophysics*, **60**, 447–458, doi: [10.1190/1.1443782](https://doi.org/10.1190/1.1443782).
- Kuo, J. T., and T. Dai, 1984, Kirchhoff elastic wave migration for the case of noncoincident source and receiver: *Geophysics*, **49**, 1223–1238, doi: [10.1190/1.1441751](https://doi.org/10.1190/1.1441751).
- Li, X.-Y., H. Dai, and F. Mancini, 2007, Converted-wave imaging in anisotropic media: Theory and case studies: *Geophysical Prospecting*, **55**, 345–363, doi: [10.1111/j.1365-2478.2007.00612.x](https://doi.org/10.1111/j.1365-2478.2007.00612.x).
- Liu, E., and A. Martinez, 2013, Seismic fracture characterization: Concepts and practical applications: EAGE Publications BV.
- Martin, G. S., R. Wiley, and K. J. Marfurt, 2006, Marmousi2: An elastic upgrade for Marmousi: *The Leading Edge*, **25**, 156–166, doi: [10.1190/1.2172306](https://doi.org/10.1190/1.2172306).
- Mavko, G., J. Dvorkin, and J. Walls, 2005, A rock physics and attenuation analysis of a well from the Gulf of Mexico: 75th Annual International Meeting, SEG, Expanded Abstracts, 1585–1588.
- McDonald, F. J., F. A. Angona, R. L. Mills, R. L. Sengbush, R. G. van Nostrand, and J. E. White, 1958, Attenuation of shear and compressional waves in Pierre shale: *Geophysics*, **23**, 421–439, doi: [10.1190/1.1438489](https://doi.org/10.1190/1.1438489).
- Shen, Y., B. Biondi, R. Clapp, and D. Nichols, 2014, Wave-equation migration *Q* analysis (WEMQA): 84th Annual International Meeting, SEG, Expanded Abstracts, 3757–3762.
- Stewart, R. R., J. E. Gaiser, R. J. Brown, and D. C. Lawton, 2002, Converted wave seismic exploration: *Methods: Geophysics*, **67**, 1348–1363, doi: [10.1190/1.1512781](https://doi.org/10.1190/1.1512781).
- Sun, J., S. Fomel, T. Zhu, and J. Hu, 2016, *Q*-compensated least-squares reverse time migration using low-rank one-step wave extrapolation: *Geophysics*, **81**, no. 4, S271–S279, doi: [10.1190/geo2015-0520.1](https://doi.org/10.1190/geo2015-0520.1).
- Sun, J., and T. Zhu, 2015, Stable attenuation compensation in reverse-time migration: 85th Annual International Meeting, SEG, Expanded Abstracts, 3942–3947.
- Sun, J., T. Zhu, and S. Fomel, 2015, Viscoacoustic modeling and imaging using low-rank approximation: *Geophysics*, **80**, no. 5, A103–A108, doi: [10.1190/geo2015-0083.1](https://doi.org/10.1190/geo2015-0083.1).
- Wang, C., J. Cheng, and B. Arntsen, 2015, Imaging condition for converted waves based on decoupled elastic wave modes: 85th Annual International Meeting, SEG, Expanded Abstracts, 4385–4390.
- Wang, C., J. Cheng, and B. Arntsen, 2016, Scalar and vector imaging based on wave mode decoupling for elastic reverse time migration in isotropic and transversely isotropic media: *Geophysics*, **81**, no. 5, S383–S398, doi: [10.1190/geo2015-0704.1](https://doi.org/10.1190/geo2015-0704.1).
- Xue, Z., J. Sun, S. Fomel, and T. Zhu, 2016, *Q*-compensated full-waveform inversion using constant-*Q* wave equation: 85th Annual International Meeting, SEG, Expanded Abstracts, 1063–1068.
- Yan, J., and P. Sava, 2008, Isotropic angle-domain elastic reverse-time migration: *Geophysics*, **73**, no. 6, S229–S239, doi: [10.1190/1.2981241](https://doi.org/10.1190/1.2981241).
- Yan, R., and X.-B. Xie, 2012, An angle-domain imaging condition for elastic reverse time migration and its application to angle gather extraction: *Geophysics*, **77**, no. 5, S105–S115, doi: [10.1190/geo2011-0455.1](https://doi.org/10.1190/geo2011-0455.1).
- Yang, P., R. Brossier, L. Mtivier, and J. Virieux, 2016, Wavefield reconstruction in attenuating media: A checkpointing-assisted reverse-forward simulation method: *Geophysics*, **81**, no. 6, R349–R362, doi: [10.1190/geo2016-0082.1](https://doi.org/10.1190/geo2016-0082.1).
- Yao, J., T. Zhu, F. Hussain, and D. J. Kouri, 2017, Locally solving fractional Laplacian viscoacoustic wave equation using Hermite distributed approximating functional method: *Geophysics*, **82**, no. 2, T59–T67, doi: [10.1190/geo2016-0269.1](https://doi.org/10.1190/geo2016-0269.1).
- Zhang, Q., and G. A. McMechan, 2010, 2D and 3D elastic wavefield vector decomposition in the wavenumber domain for VTI media: *Geophysics*, **75**, no. 3, D13–D26, doi: [10.1190/1.3431045](https://doi.org/10.1190/1.3431045).
- Zhang, Y., and J. Sun, 2009, Practical issues in reverse time migration: True amplitude gathers, noise removal and harmonic source encoding: *First Break*, **27**, 53–59, doi: [10.3997/1365-2397.2009002](https://doi.org/10.3997/1365-2397.2009002).
- Zhang, J., J. Wu, and X. Li, 2013, Compensation for absorption and dispersion in prestack migration: An effective *Q* approach: *Geophysics*, **78**, no. 1, S1–S14, doi: [10.1190/geo2012-0128.1](https://doi.org/10.1190/geo2012-0128.1).
- Zhang, Y., P. Zhang, and H. Zhang, 2010, Compensating for viscoacoustic effects in reverse-time migration: 80th Annual International Meeting, SEG, Expanded Abstracts, 3160–3164.
- Zhou, J., S. Birdus, B. Hung, K. H. Teng, Y. Xie, D. Chagalov, A. Cheang, D. Wellen, and J. Garrity, 2011, Compensating attenuation due to shallow gas through *Q* tomography and *Q* PSDM: A case study in Brazil: 81st Annual International Meeting, SEG, Expanded Abstracts, 3332–3336.
- Zhu, T., 2014, Time-reverse modeling of acoustic wave propagation in attenuating media: *Geophysical Journal International*, **197**, 483–494, doi: [10.1093/gji/gjt519](https://doi.org/10.1093/gji/gjt519).
- Zhu, T., 2015a, Viscoelastic time-reversal imaging: *Geophysics*, **80**, no. 2, A45–A50, doi: [10.1190/geo2014-0327.1](https://doi.org/10.1190/geo2014-0327.1).
- Zhu, T., 2015b, Wave propagation and wavefield reconstruction in viscoelastic media: 85th Annual International Meeting, SEG, Expanded Abstracts, 3972–3976.
- Zhu, T., 2016, Implementation aspects of attenuation compensation in reverse-time migration: *Geophysical Prospecting*, **64**, 657–670, doi: [10.1111/1365-2478.12301](https://doi.org/10.1111/1365-2478.12301).
- Zhu, T., and J. M. Carcione, 2014, Theory and modeling of constant-*Q* P- and S-waves using fractional spatial derivatives: *Geophysical Journal International*, **196**, 1787–1795, doi: [10.1093/gji/gjt483](https://doi.org/10.1093/gji/gjt483).
- Zhu, T., and J. M. Harris, 2015, Improved seismic image by *Q*-compensated reverse time migration: Application to crosswell field data, West Texas: *Geophysics*, **80**, no. 2, B61–B67, doi: [10.1190/geo2014-0463.1](https://doi.org/10.1190/geo2014-0463.1).
- Zhu, T., J. M. Harris, and B. Biondi, 2014, *Q*-compensated reverse-time migration: *Geophysics*, **79**, no. 3, S77–S87, doi: [10.1190/geo2013-0344.1](https://doi.org/10.1190/geo2013-0344.1).